Progress in Oceanography 205 (2022) 102817

Contents lists available at ScienceDirect

Progress in Oceanography

journal homepage: www.elsevier.com/locate/pocean

Internal wave breaking near the foot of a steep East-Pacific continental slope

Hans van Haren [a,*], Gunnar Voet [b], Matthew H. Alford [b], Daniel J. Torres [c]

[a] Royal Netherlands Institute for Sea Research (NIOZ), P.O. Box 59, 1790 AB Den Burg, the Netherlands
[b] Scripps Institution of Oceanography, UC San Diego, Mail Code 0213 La Jolla, CA 92093-0213, USA
[c] Woods Hole Oceanographic Institution, MS #30, 266 Woods Hole Road, Woods Hole, MA 02543, USA

ARTICLE INFO

Keywords:
Pacific Ocean
Sloping topography
High-resolution instrumentation
Internal wave breaking
High turbulence intensity near seafloor

ABSTRACT

The sloping sides of ocean basins are of particular interest for their potential importance for considerable turbulence generation via internal wave breaking and associated water circulation. The difference with the ocean interior may be manifest in a 10–100 m relatively thin layer above the seafloor. We set up an observational study with high-resolution stand-alone instrumentation attached to a custom-made release-anchor frame sampling to within 0.5 m from the seafloor up to 150 m above it. For two months, the taut wire moored instrumentation was tested in 1100 m water depth of the East-Pacific, off the coast of San Diego (CA, USA). The mooring was oceanward of an underwater bank and near the foot of its steep but gentle two-dimensional slope. Temperature sensor data demonstrate that internal waves peak at semidiurnal frequencies. While short (<1 h) periods show complicated structure, tidally averaged turbulence dissipation rate monotonically increases towards the seafloor over two orders of magnitude. The largest turbulence dissipation rates are observed during the relatively warm phase of an internal wave. Although the local topographic slope is supercritical for semidiurnal internal waves, turbulent bores propagating up the slope and hydraulic jumps are not observed. Most of the turbulence appears to be dominated by shear production, but not related to steady frictional flow near the seafloor.

1. Introduction

The omnipresent underwater sloping topography has important consequences for the water circulation in the ocean. Its effects on the generation of small-scale turbulence, thereby affecting the redistribution of suspended matter and life, have been the subject of many oceanographic studies on the relevant processes since suggestions made by Munk (1966) and Armi (1978). For the circulation of water in a confined basin, the seafloor boundary is of particular interest because the small-scale turbulence is expected to be different than in the basin interior.

Above a flat seafloor this is understood from the concept of a bottom-frictional shear flow, thereby creating a near-homogeneous 'bottom boundary layer' (Prandtl, 1905) O(1 −1 0) m in height and modified by the rotation of the Earth (Ekman, 1905).

Above a sloping seafloor, the bottom-frictional flow concept may create a complex flow structure due to the effects of buoyancy because the ocean is generally vertically stably stratified in density (e.g., Garrett, 1990). This results in a complex circulation in the boundary layer as well as in the ocean. Depending on the level of efficiency of turbulent mixing, i.e. on the level of restratification, the vertical profile of turbulent flux determines the direction of interior flow, with opposing results in different scenarios (Munk, 1966; Ferrari et al., 2016). In all scenarios, the bottom-normal turbulent flux goes to zero at the seafloor as in the Prandtl-Ekman-concept of a frictional-shear-flow bottom boundary layer.

However, the same density stratification supports inertio-gravity waves (henceforth 'internal waves' in short) that may break on the sloping topography. Such internal wave breaking above sloping topography will occur episodically within a wave period so that, (1) the waters just above the seafloor will restratify quasi-continuously and a permanent near-homogenous bottom boundary layer will not exist, (2) the turbulence will be efficient all the way to the seafloor, (3) turbulent overturning may not necessarily be shear-driven but can also be convection-(buoyancy)-driven and across a larger distance from the seafloor, in comparison with turbulence via steady bottom-frictional flow, as modelled by Gemmrich and Klymak (2015), (4) the water circulation will be completely different from one that is governed by a bottom-

* Corresponding author.
E-mail address: hans.van.haren@nioz.nl (H. van Haren).

https://doi.org/10.1016/j.pocean.2022.102817
Received 15 November 2021; Received in revised form 25 March 2022; Accepted 16 May 2022
Available online 19 May 2022

frictional flow as internal waves and turbulence are essentially three-dimensional phenomena.

Deep-sea observational evidence for points (1) to (3) have been given by Thorpe (1987) who used 10-m spaced moored sensors down to 10 m from the seafloor, by van Haren (2006) who used 0.5 m spaced sensors down to 1.7 m from the seafloor and by van Haren and Gostiaux (2012) who used 0.5 m spaced sensors down to 0.5 m from the seafloor. Moored observations were compared with extensive shipborne microstructure temperature- and shear-probe turbulence profiler data obtained by van Haren et al. (1994) to within 0.15 m using a protective cage around the sensors (Dewey et al., 1987). All above sampling near sloping seafloors demonstrated negligible or small (<3 m in height) mixed layer, with a high mixing efficiency >0.2 as far as could be judged from the coarse distribution of results (van Haren et al., 1994).

To establish the relative importance of bottom-frictional and internal-wave-generated turbulence intensities on the governing water circulation above sloping topography in point (4), a large modeling and observational project 'Boundary Layer Turbulence BLT' was created. The hypothesis is that above sloping topography internal wave breaking is the dominant process in generating turbulence, both at the seafloor as well as at heights extending between 10 and 100 m above the seafloor. It is also hypothesized that a thin layer of weaker turbulence near the seafloor satisfies the no-density flux condition that leads to upwelling flow in a thin 'boundary layer' to balance the sinking in the stratified ocean interior due turbulent mixing there. For the observational part, instrumentation will be used that provides state-of-the-art data, including from extensive shipborne microstructure profiling, modular acoustic velocity sensors and high-resolution temperature 'T-'sensors, over the entire internal wave range and reaches to well within the frictional boundary, if existent.

In this paper, we present results from a test experiment to investigate the dominance of particular turbulence processes near a gentle two-dimensional but steep slope via T-sensor observations using moored instrumentation to within 0.5 m above a seafloor of the East Pacific. The test experiment is held in the San Diego Trough, offshore of San Diego, CA, USA. The area is known for substantial bottom-trapped internal tides Pinkel and Alford, 1999). The region's internal tides are generally closely phase-locked to the surface tide, implying strong local generation as found by Ponte and Cornuelle (2013), but remotely incident waves also play a role (Mazloff et al., 2020). Internal tide motions in somewhat shallower water nearby (Lerczak et al, 2003) have relatively short horizontal wavelengths of 5 and 8 km in cross- and along-slope directions, respectively. The horizontal wavelengths are similar to the sizes of (sub-)mesoscale eddies in the area, as observed in surface currents using 250-m grid radar (Kim, 2010).

2. Site, data handling and methods

2.1. Custom-made small release-frame for near-bottom studies using moored instrumentation

Standard deep-sea mooring lines are instrumented to within about 5 to 10 m from the seafloor to allow for acoustic releases and some chain/cable between the lowest instrument and the anchor weight. This avoids potential entanglement of the acoustic release(s) with unknown seafloor debris like large boulders in rugged terrain and artificial waste disposal. It is also expected to provide sufficient room for slackening after landing of the anchor weight at the seafloor before the buoyancy stretches the mooring cable. However, it prevents sampling the most interesting part just above the seafloor in bottom boundary layer studies. When the seafloor is mapped in detail prior to mooring deployment, for example via side-scan sonar or underwater video, the risk of entanglement may be reduced by choosing a relatively flat, smooth-textured seafloor.

Technically, a common means to bring instrumentation close to the seafloor is by mounting them on structures called 'bottom-landers'. Such structures have the disadvantage of being generally quite bulky thereby disturbing the flow of interest, and yet despite being relatively small, less than 6 m in height to be handled from a ship during an overboard operation, they are unable to resolve the entire range of near-bottom turbulence motions. For studies on <10 m tall bottom-frictional and up to 100 m tall internal wave breaking turbulent overturning events, standard mooring lines and structures are not adequate.

For the present study, we designed a small and slender frame that can hold two acoustic releases with a 0.4 m chain between the release-links (Fig. 1a). The chain goes through a 0.2 m long U-shaped steel gutter underneath two round bars. The gutter can be welded (or fixed) on any steel (or other material) anchor weight. The <0.1 m free space for slackening is considered to be sufficient for a > 2 kN net-buoyant mooring line that lands with a speed between 1 and 1.5 m s^{-1} at the seafloor. As deep-sea acoustic releases are about 1 m in length, the entire frame-releases-anchor weight is about 1.5 m tall. The custom-made frame however can also hold small equipment like T-sensors that can be mounted on a steel bar on its outside. In doing so, a string of T-sensors normally attached to a cable under a sub-surface buoy, as also employed here, can be extended to the level of the acoustic release hooks, about 0.5 m from the seafloor if the seabed is sandy and not too muddy or fluffy.

2.2. Mooring location and instrumentation

On 12 September 2019, the release-frame T-sensor mooring was deployed at 32° 37.03′N, 117° 28.39′W, 1086 m water depth off the coast of San Diego, CA, USA in the East-Pacific (Fig. 1b). The local inertial frequency $f = 7.86 \times 10^{-5}$ $s^{-1} = 1.08$ cpd (cycles per day) at this site that is located just poleward of the diurnal frequency K_1 critical latitude. Current measurements were made every 10 min in time and every 4 m vertically using a downward looking 300 kHz Teledyne/RDI acoustic Doppler current profiler (ADCP) that was mounted in the top buoy of a mooring in slightly shallower waters about 900 m to the southeast of the T-sensor mooring. In this test experiment we did not have more ADCP's available to mount in every mooring. Unfortunately, the ADCP delivered good data only to about 970 m. The top buoy provided 4 kN buoyancy, so that mooring deflections were minimal, <0.1 m vertically, under maximum 0.15 m s^{-1} current-flow speeds.

The two taut-wire moorings were above a relatively smooth topographic slope, about 500 m, i.e. less than one internal tidal wavelength, horizontally from the foot of the slope into a nearly flat basin some 100 m deeper. The slope was nearly two-dimensional and less incised by small canyons than the steeper slopes higher-up. Locally, the seafloor slope was about 0.14 (8°) which is significantly steeper or 'supercritical' than the slope of propagating semidiurnal internal tides (e.g., LeBlond and Mysak, 1978) that amounts to 0.05 (3°) for the large-scale mean buoyancy frequency $N = 2.4 \times 10^{-3}$ $s^{-1} = 33$ cpd. The moorings were recovered nearly two months after deployment, on 06 November 2019.

A total of 102 'NIOZ4′ self-contained temperature 'T' sensors were used sampling at a rate of 1 Hz, with precision better than 5×10^{-4} °C and a noise level of about 6×10^{-5} °C (van Haren, 2018). Sensors were taped at vertical intervals of $\Delta z = 0.5$ m with the lowest two T-sensors on the release frame, at $\Delta z = 1.0$ m (T-sensors 3 to 51) and at $\Delta z = 2.0$ m intervals (upper 51 T-sensors) to a 150 m long, 6.3 mm diameter nylon-coated steel cable. The T-sensors were synchronized via induction every 4 h. Thus, each entire vertical profile of 150 m was measured in less than 0.02 s.

2.3. Processing T-sensor data

Three T-sensors showed some noise problems and are not further considered. Their data are interpolated. Due to unknown reasons about half the T-sensors showed data-spikes. During post-processing the data from all T-sensors are subjected to the same spike-removal procedure, which implies effective low-pass filtering with a cut-off frequency at about $\omega = 2000$ cpd. As a result, a frequency range of nearly two orders

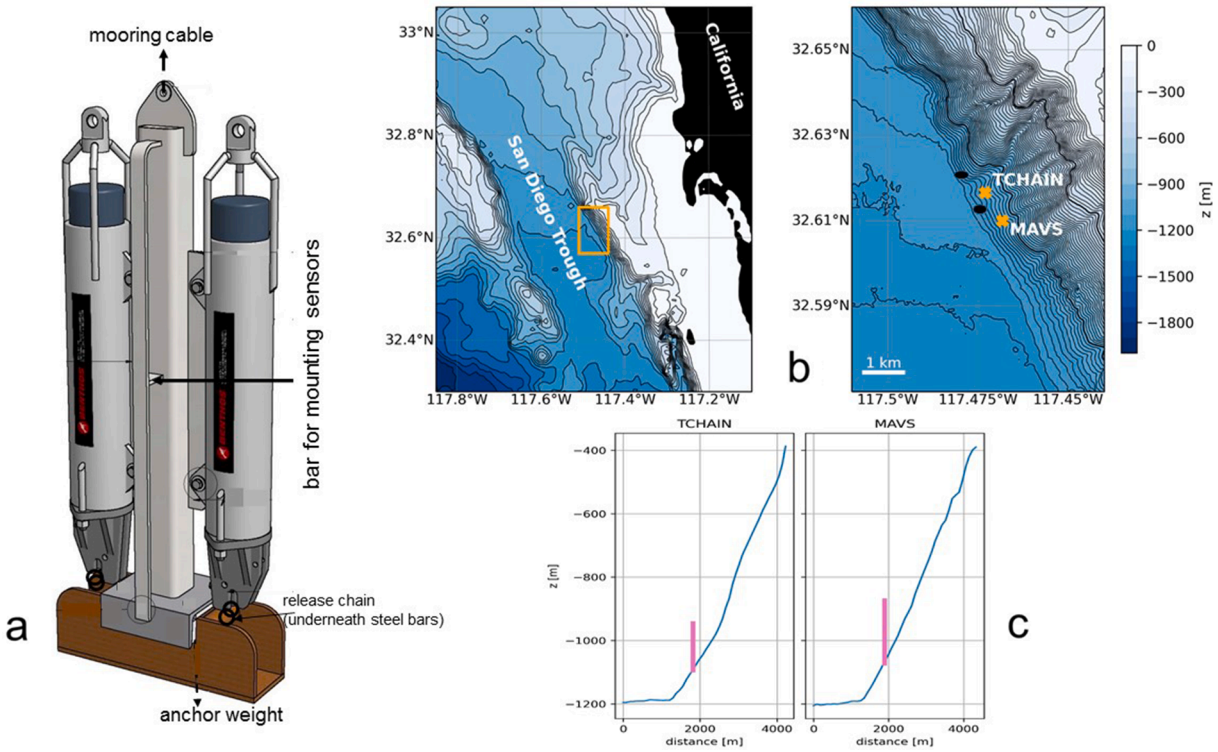

Fig. 1. (a) Custom-made small release-frame to be welded or mounted on an anchor-weight and to be attached under an ocean-mooring cable. (b) Bathymetry of East-Pacific continental slope offshore San Diego (CA, USA), with mooring locations. TCHAIN indicates the high-resolution temperature sensor mooring, MAVS indicates the mooring with the downward looking acoustic Doppler current profiler in the top-buoy. Bathymetry from 1/3 Arc-second NAVD 88 Coastal Digital Elevation Model of NOAA (https://www.ncei.noaa.gov/metadata/geoportal/rest/metadata/item/gov.noaa.ngdc.mgg.dem:3542/html, last accessed 14 November 2021). (c) Cross-slope sections of bathymetry through the mooring sites.

of magnitude is still resolved at super-buoyancy frequencies. In this frequency range, the transition from anisotropic stratified to isotropic homogeneous turbulence is expected (D'Asaro and Lien, 2000).

An important post-processing feature of the T-sensors is the correction for instrumental drift. As outlined in van Haren (2018) the drift-correction is applied on a section of typically 4 days of data, of which the mean profile is forced to a polynomial fit, as the mean profile has to be statically stable and smooth by nature when the averaging is over at least the local inertial period. The polynomial fit may be compared with mean CTD-data, if available. For the present data, this procedure was slightly changed by accommodating for the non-equidistant T-sensors and because the lowest T-sensor is closer to the seafloor than the local CTD-data.

The moored observations are supported by shipborne SeaBird Electronics SBE-911 Conductivity Temperature Depth CTD-profiles in the area, to within 5 m vertically from the seafloor and 1 km horizontally from the mooring sites (Fig. 1). The CTD-data are used to establish a local, preferably linear, temperature-density relationship to be able to compute turbulence values form the moored T-sensor data.

During post-processing, the T-sensor data are transferred to conservative temperature (Θ) values (IOC et al., 2010) mainly to correct for pressure effects. Over a range of 200 m above the seafloor, Θ are used as a tracer for variations in potential density anomaly referenced to a level of 1000 dbar (σ_1) following a tight, constant linear relationship obtained from CTD-data (Fig. 2),

$$\delta\sigma_1 = \alpha\delta\Theta \qquad (1)$$

with $\alpha = -0.1893 \pm 0.0005$ kg m^{-3}°C^{-1} denoting the regression coefficient under local conditions (Fig. 2d).

Turbulence values are obtained using the moored T-sensor data by calculating 'overturning' scales. These scales follow after reordering every 1 s the 150 m high potential density (Conservative Temperature) profile $\sigma_1(z)$, which may contain inversions, into a stable monotonic profile $\sigma_1(z_s)$ without inversions (Thorpe, 1977). After comparing observed and reordered profiles, displacements $d = \min(|z - z_s|)\cdot\mathrm{sgn}(z - z_s)$ are calculated necessary for generating the reordered stable profile. Certain tests apply to disregard apparent displacements associated with instrumental noise and post-calibration errors (Galbraith and Kelley, 1996). Such a test-threshold is very low for NIOZ-temperature sensor data, $<5 \times 10^{-4}$°C (van Haren, 2018). Then,

$$\varepsilon = 0.64 d^2 N^3 \qquad (2)$$

the turbulence dissipation rate, where N denotes the local buoyancy frequency computed from each of the reordered, essentially statically stable, vertical density profiles. The numerical constant follows from empirically relating the root-mean-square 'rms' overturning scale $L_T = d_{rms} = (1/n\Sigma d^2)^{0.5}$ over n samples with the rms Ozmidov-scale of largest isotropic turbulence overturns in a stratified fluid $L_O = (\varepsilon/N^3)_{rms} = 0.8L_T$ (Dillon, 1982).

In (2) we use individual d to replace overturning scales, instead of taking their rms-value across a single overturn as originally proposed by Thorpe (1977). The reason is that we cannot easily distinguish individual overturns, first, because overturns are found at various scales with small ones overprinting larger overturns, and, second, because some overturns exceed the range of T-sensors. Instead, we first calculate non-averaged d in (2) for high-resolution images of ε(z, t). Subsequently, we calculate 'mean' turbulence values by averaging the parameters in the vertical [·] or in time ⟨⟩, or both. The 1-Hz sampling of moored T-sensor profile data allows sufficient averaging over all different turbulence characteristics.

The errors in mean turbulence values thus obtained depend on the error in N, the error in the temperature-density relationship while the

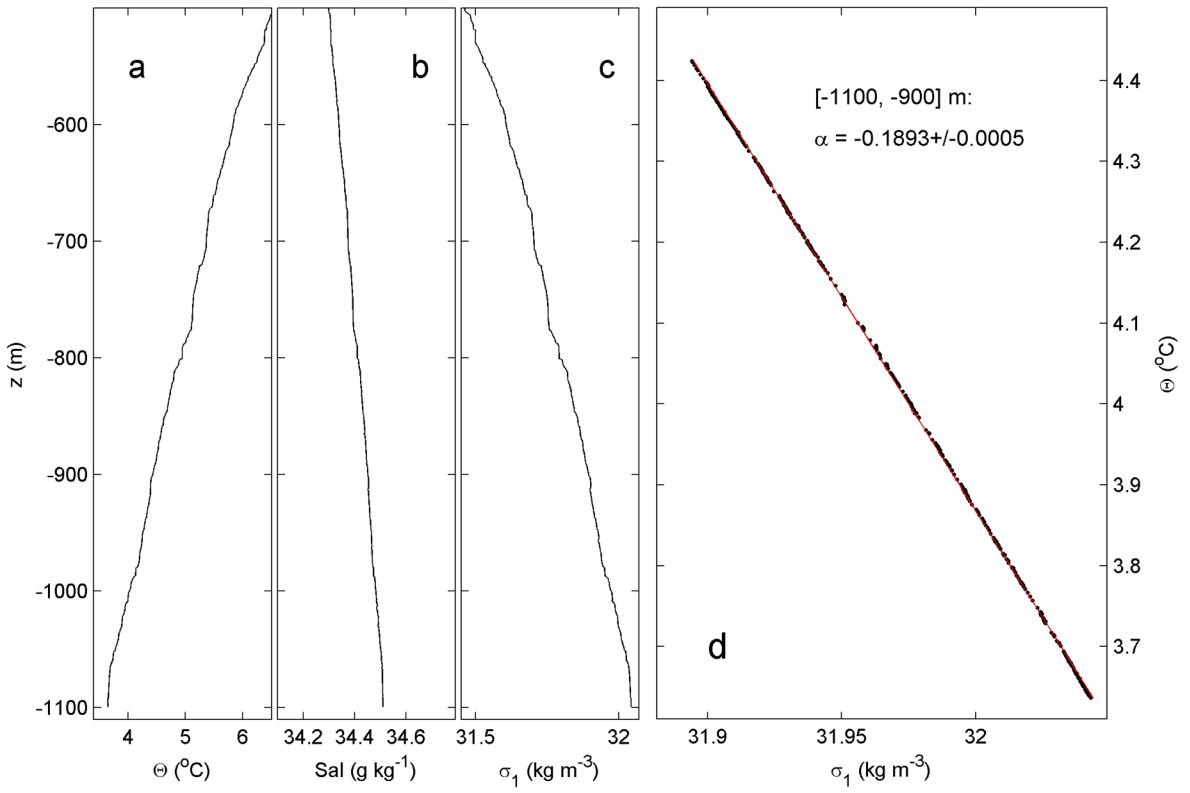

Fig. 2. Shipborne CTD-observations down to 5 m above the seafloor to within 1 km horizontally from the temperature sensor mooring, obtained during the day of mooring deployment. (a) Conservative Temperature. (b) Absolute Salinity. The x-axis range approximately corresponds with that in a. in terms of density contributions. (c) Density anomaly referenced to 1000 dbar. (d) Conservative Temperature-density anomaly (referenced to 1000 dbar) relationship, from the lower 200 m of the CTD-profile.

instrumental noise error of the thermistors is negligible. Given the errors, the uncertainty in time-depth mean dissipation rates amounts about a factor of two, which is the minimum error range for turbulence values (Oakey, 1982). Smaller uncertainties are not possible using measurements in natural waters where turbulence values from individual overturns vary over four orders of magnitude (e.g., Oakey, 1982; van Haren and Gostiaux, 2012; Gregg et al., 2018). Using similar T-sensor data from above Great Meteor Seamount, van Haren and Gostiaux (2012) found turbulence values to within a factor of three similar to those inferred from ship-borne CTD/LADCP profiler data near the seafloor. Their values compare well with profiler-based estimates in similar sloping bottom areas by Klymak et al. (2008).

It has been argued that L_O/L_T should not be a constant but varies as a function of stratification, stage, time-evolution and type of turbulence generation (e.g., Smyth et al., 2001; Chalamalla and Sarkar, 2015; Mater et al., 2015; Mashayek et al., 2022). The functional varying reflects the one order of magnitude of variations as observed in microstructure ocean data (e.g., Oakey, 1982; Dillon, 1982). While such varying ratio is acknowledged for specific conditions such as for instance pure convection or low Reynolds number flows, there are several reasons why it may not apply, and cannot be applied, to the present ocean data. The moored high-resolution T-sensor data provide a priori insight in particular internal wave turbulence processes, but we are not primarily concerned with individual overturning values. Instead we calculate suitably averaged turbulence values, as detailed below. In any given high Reynolds number environment like the deep ocean, shear- and buoyancy-driven turbulence intermingle and are hard if not impossible to separate. Examples of numerical modelling studies of particular stages of instability developments show that a finger of convective instability develops secondary shear instability along its fringe (Li and Li, 2006), while the roll-up stage of shear instability develops secondary convective instability mushrooms (Matsumoto and Hoshino, 2004). Comparison between calculated turbulence values using shear measurements and using Thorpe overturning scales with mean $L_O/L_T = 0.8$ from areas with such mixtures of turbulence development above sloping ocean topography led to consistent results (Nash et al., 2007). This is not surprising given the important and rapid restratification during internal wave breaking above steep slopes, as reported from numerical modelling (e.g., Slinn and Riley, 1996; Winters, 2015) and ocean observations (e.g., Thorpe, 1987; van Haren and Gostiaux, 2012). Thus, from the arguments above and the reasoning in Mater et al. (2015), internal wave breaking unlikely biases turbulence dissipation rates computed from Thorpe overturning scales by more than a factor of two to three, provided some suitable time–space averaging is performed instead of considering single profiles. This factor of two to three is within the range of our error.

3. Observations

Although Conservative Temperature is presented and used throughout, we will henceforth refer to it in the text as ‘temperature’ for short.

3.1. Vertical temperature profiles

The two CTD profiles obtained during the deployment and recovery cruises two months apart were not obtained at precisely the same location (Fig. 1b). Nevertheless, they largely show the same structure of the vertical temperature profile with an overall steady decrease with increasing depth and many small-scale steps of alternating more and less vertical temperature change (stratification) and episodic temperature inversions. Near the seafloor, temperature stratification seems less than higher-up in the profile obtained during the first cruise, but not in the profile obtained during the second cruise. These few profiles already

demonstrate a lack of a homogeneous bottom-boundary-layer above sloping topography in an environment strongly flushed by internal waves. The difference in profiles between the two cruises is largely due to the temporal variability of, e.g., internal waves and eddies passing. This becomes clear when the profiles are plotted as height above the seafloor (Fig. 3b). The temporal variability may be inferred from the subsampled set of vertical profiles of the first day of T-sensor mooring. Their smooth polynomial-fit mean value generally fits the large-scale vertical structure of the CTD-profiles.

3.2. Two-month time series

On the large timescale of the two months of the entire moored observations record, the temperature variability is clearly visible (Fig. 4a). Semidiurnal tidal variations demonstrate vertical excursions of 100 m crest-to-trough. It is obvious that such large excursions can only be attributed to baroclinic internal waves, as the barotropic surface tidal excursions that dominate the ADCP's pressure record are more than one-and-a-half orders of magnitude smaller (the white line vertically shifted but on scale in Fig. 4a; and Fig. 4e). While the pressure record shows a spring-neap cycle and distinct diurnal tides that are evidence of quasi-deterministic signals governed by the moon-sun system (Fig. 4e), the temperature excursions peak only around the semidiurnal lunar frequency. Equally large vertical isotherm excursions as those of the internal tide are observed on the slower timescales of weeks and months.

Although the semidiurnal tidal periodicity is dominantly visible in the temperature time-depth record, it is not obvious in the time series of vertically averaged turbulence dissipation rates (Fig. 4b). Both the time series for turbulence near the seafloor (purple graph) as higher-up (light-blue graph) in the observed range show the same lack of (semidiurnal) tidal periodic variations with time. As will be demonstrated below in detailed observations, the turbulence occurs in bursts that are related not only to tidal phases but also to non-linear modification by interaction with stratification and higher frequency internal waves near N. Per record, the vertically averaged values cover a range of four orders of magnitude, commensurate previous ocean turbulence observations (e.g., Oakey, 1982; Gregg, 1987). On average, the record of turbulence dissipation rate near the seafloor shows one order of magnitude larger values than the record from higher-up in the moored T-sensor line.

The noise-filtered current records (Fig. 4c,d) do show semidiurnal tidal periodicity, but more akin to the temperature excursion record than to the (barotropic surface) pressure record (Fig. 4e) as distinct-dominant spring-neap cycle is lacking in the former two. Horizontal flows are relatively weak, with maximum values of 0.15 m s^{-1}, while vertical motions are slightly downward in the mean with minimum values of -0.01 m s^{-1} or -1000 m d^{-1}. The pressure record (Fig. 4e) is dominated by the surface tide, with a spring-neap modulation including spring-tide around days 255, 270, 285 and 300, with the ones around days 270 and 300 monthly enhanced.

3.3. Two-day time-depth series

Two examples of two-day, 150-m time-depth series of temperature and turbulence dissipation rate are presented to demonstrate the variability of the two-month time series above the supercritical slope near the transition of sub-critical slope deeper down.

The first example in Fig. 5 shows >100 m large tidal excursions with downward peaks during the warming phase. Strong fronts at the transition from warming to (upslope moving) cooling phase as in, e.g., Hosegood et al. (2004) are not observed, but internal tidal waves are not sinusoidal (Fig. 5a) and episodic peaks in turbulence dissipation rate do occur around the warmest phase in the semidiurnal period (Fig. 5b). Then, enhanced turbulence dissipation rate extends up to 80 m above the seafloor, highly depending on the particular tidal period. Turbulence seems mainly shear-induced, as suggested by the roll-over forms in detailed temperature record (Fig. 5d) resembling Kelvin-Helmholtz instabilities. This dominance of shear-induced over convection-induced turbulence will be verified from spectral analysis below. Largest overturns provide unstable vertical temperature profiles lasting about an hour, which is close to the local large-scale buoyancy period. The two-

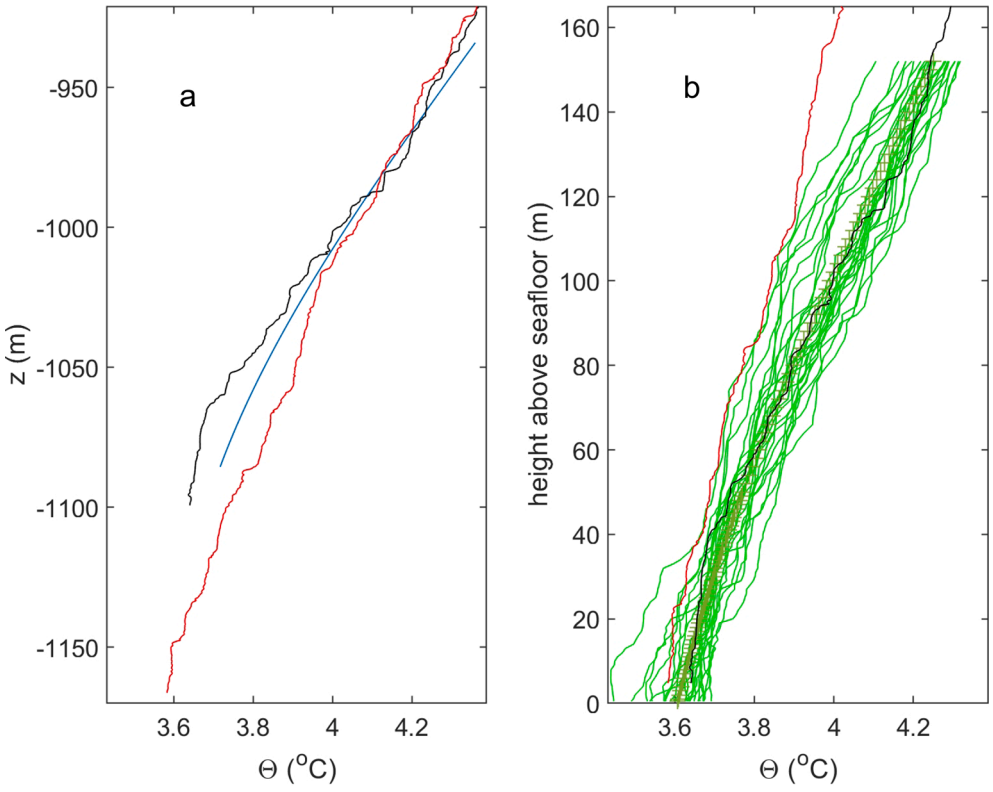

Fig. 3. Vertical temperature profile comparison between shipborne CTD and moored T-sensors. (a) Two CTD-profiles down to 5 m above the seafloor, obtained during the day of mooring deployment (black) and mooring recovery (red). The blue line is the smooth third-order polynomial for drift correction through the mean of T-sensor values for the first day after deployment. (b) Detail of a., with the two CTD-profiles now with reference to the local seafloor, with the blue crosses indicating the smooth mean fit and the green lines individual T-sensor profiles every hour. (For interpretation of the references to colour in this figure legend, the reader is referred to the web version of this article.)

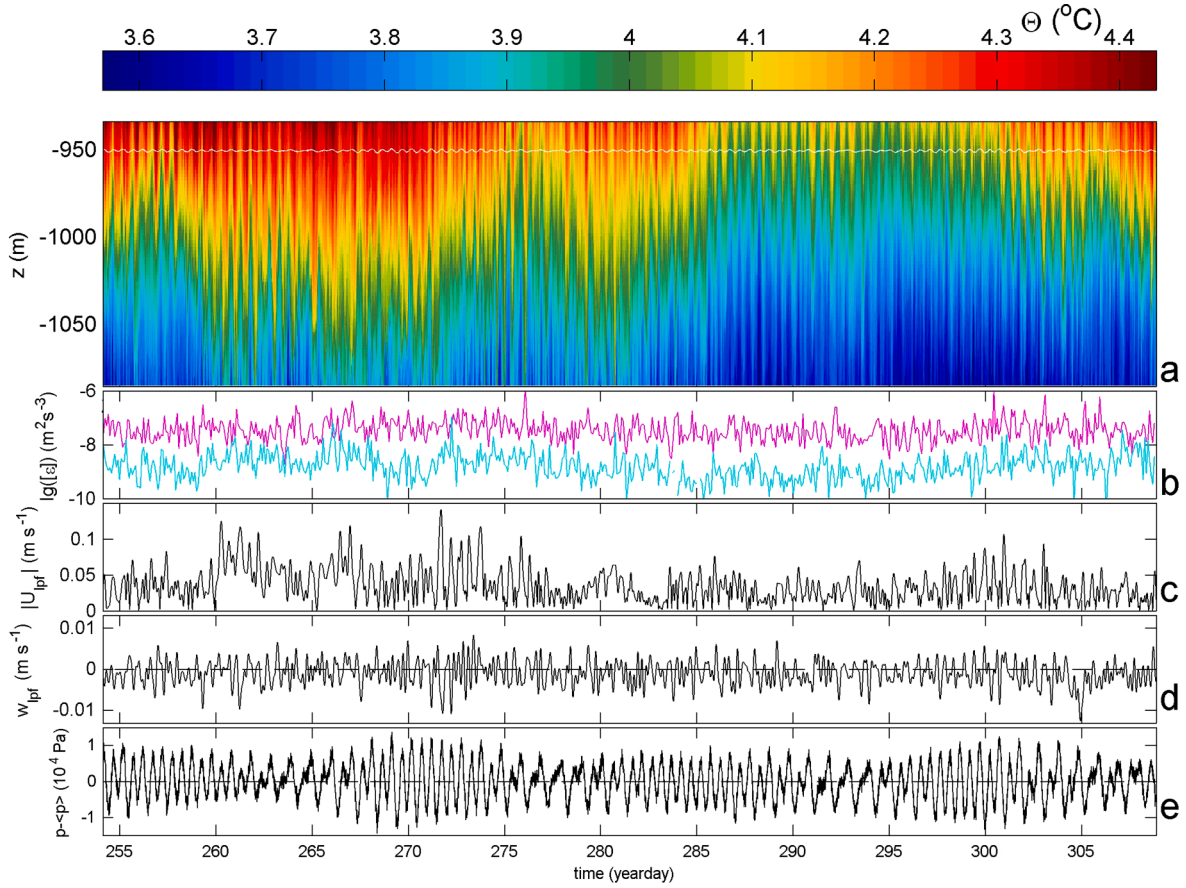

Fig. 4. Nearly two months of moored data overview. (a) Depth-time series of Conservative Temperature from T-sensor data. The seafloor is at the horizontal axis. The white line shows the pressure record of the ADCP, arbitrarily shifted vertically. (b) Logarithm of vertically and 3-h averaged dissipation rate from T-sensor data, for the upper 30 T-sensors (light-blue) and the lower 30 T-sensors (purple). (c) Three-hourly low-pass filtered current magnitude from ADCP-data at z = -960 m at the MAVS-mooring. (d) As c., but for the vertical current component. (e) (Unfiltered) ADCP-pressure record from a., relative to its time mean.

day time and 150-m depth mean value is $[\langle\varepsilon\rangle] = 3.7 \pm 1.5 \times 10^{-8}$ m^{2}s^{-3}. This mean turbulence dissipation rate works against a mean buoyancy frequency from reordered profiles of $[\langle N\rangle] = 2.2 \pm 0.1 \times 10^{-3}$ s^{-1} or a mean buoyancy period $T_N = 2\pi/N$ of about 3000 s as calculated from the reordered $T(z_s)$. The stratification is larger near the upper part of the range of T-sensors (Fig. 5c), with most turbulence in the lower 25 m above the seafloor (Fig. 5b).

The second example in Fig. 6 shows about 30 m tall internal wave excursions that are not varying with the semidiurnal period but with quarter diurnal period. This affects the turbulence dissipation rate, which is again largest in the lower 25 m above the seafloor but in this example adopting a quasi-quarter-diurnal periodicity. Episodically, turbulence dissipation rate peaks up to about 50 m above the seafloor and distinct near-bottom fronts are again lacking. Compared to Fig. 5, the two-day time and 150-m depth mean value is slightly smaller $[\langle\varepsilon\rangle] = 2.5 \pm 1 \times 10^{-8}$ m^{2}s^{-3} and works against slightly larger $[\langle N\rangle] = 2.5 \pm 0.1 \times 10^{-3}$. As in Fig. 5, large turbulent overturning roughly coincides with the warmest phase of the internal wave passing, and seems predominantly shear-driven judging from the temperature overturning pattern. No clear convective turbulence columns are observed and support is provided below using spectral analysis.

As visual inspection of the time-depth series only provides a qualitative impression of the turbulence generation type, and we do not have accurate shear measurements in the same mooring over the range of T-sensors, we compute mean temperature variance spectra and investigate the spectral continuum slopes at super-buoyancy frequencies below.

3.4. Frequency distributions

Overall variance spectra using two-month time series that are sampled (ADCP-data) and sub-sampled (T-sensor data) at 10 min intervals confirm the time-depth series observations in the dominance of semidiurnal signals in temperature variance and kinetic energy, and the lack thereof in vertical mean turbulence dissipation rates computed over data from 30 T-sensors (Fig. 7). The spectra of mean turbulence dissipation rate have a fairly featureless appearance, with a flat horizontal slope for frequencies $\omega < 6$ cpd, and a weak slope of about -0.5 (in the log–log plot) for $\omega > 6$ cpd and including N. It is noted that the one order of magnitude difference in mean turbulence dissipation rate between upper and lower range of T-sensor data (cf., Fig. 4b) causes two orders of magnitude difference in variance, apparently similarly distributed over all frequencies.

In temperature spectra, and somewhat less in those of kinetic energy, sub-peaks are observed at near-inertial/diurnal frequencies and at super-harmonic terdiurnal (interaction frequency between near-inertial/diurnal and semidiurnal motions), quarter diurnal and further, up to about eighth-diurnal for temperature near the seafloor. The energy at these distinct higher harmonic frequencies is apparently not smeared into the internal wave band continuum, as occurred at higher internal wave frequencies. The kinetic energy spectrum is flat, representing white noise, for $\omega > 20$ cpd due to instrumental noise.

Temperature variance is larger at inertial/diurnal and semidiurnal frequencies in the upper range of T-sensors compared with the lower range, about equal in variance throughout the vertical range near the buoyancy frequency, and larger in the lower range near the seafloor than

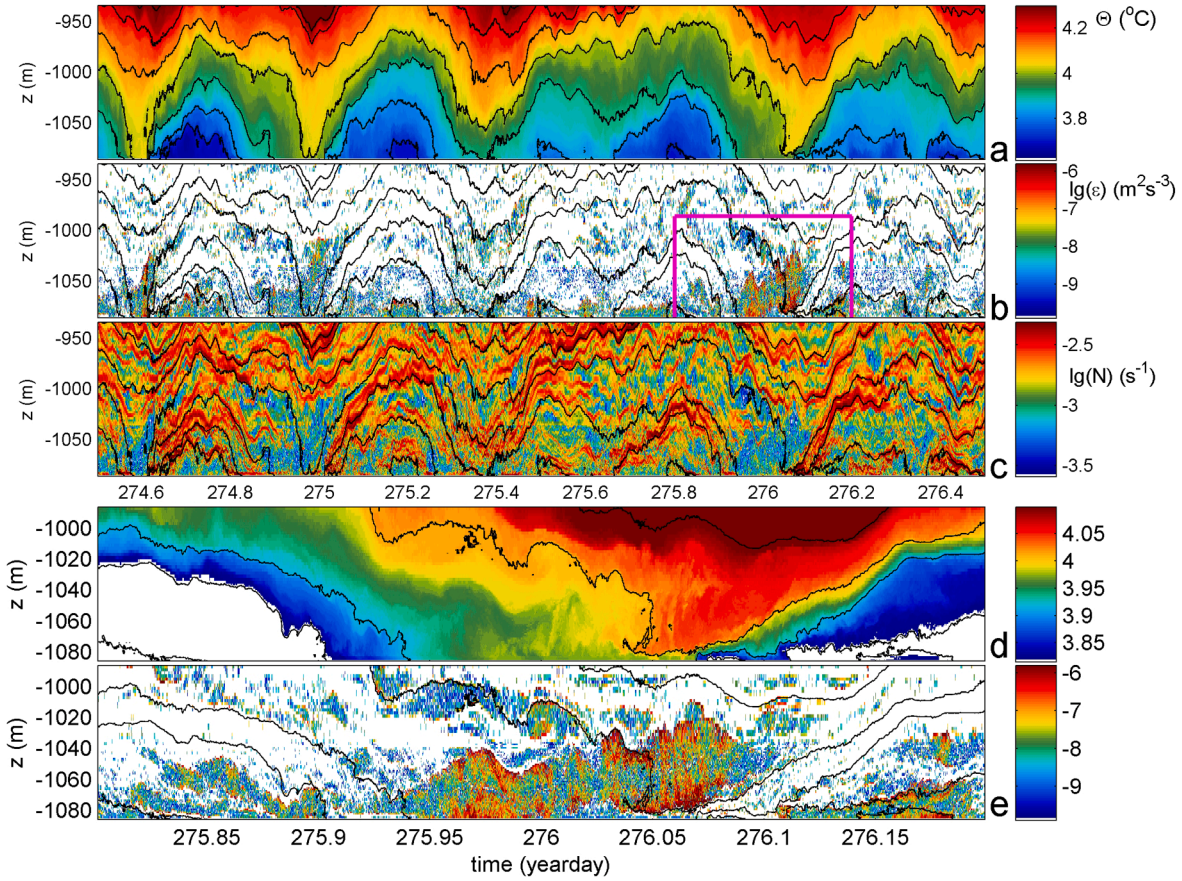

Fig. 5. Magnifications of time-depth series of moored T-sensor data around a near-bottom strong internal wave turbulence event embedded in predominant semidiurnal tidal-period motions. (a) Two days and 150 m time-depth plot of Conservative Temperature with black contours every 0.1 °C. The seafloor is at the horizontal axis. (b) Logarithm of dissipation rate from data in a., with the same black contours for reference. The purple bar indicates the period of d,e. (c) Logarithm of buoyancy frequency from (reordered) data in a. (d) As a., but for a 10-h and 90-m magnification, with different colour range but the same black contours. (e) As d., but for the logarithm of dissipation rate.

in the upper range at all other internal wave and turbulence frequencies. The precise internal wave and turbulence frequency ranges are not well determined due to the dynamic variability of the internal wave medium, i.e. the 'background' stratification that varies in space and time. In the mean, freely propagating internal waves are found in the frequency band $f \leq \omega \leq N$. Within this frequency range the upper and lower T-sensor spectra show quite different slopes.

Outside the tidal frequencies, which are not considered in general internal-wave-scaling laws (Garrett and Munk, 1972), the upper T-sensor spectrum roughly follows an overall −2 slope (Fig. 7), the canonical slope, or ω^{-2} scaling law, for a saturated internal wave field (Munk, 1981). The present spectrum demonstrates relatively strong nonlinear interactions between inertial and semidiurnal tidal harmonic frequencies in the ter-diurnal and fifth-diurnal peaks, as also observed in, e.g., the Bay of Biscay above a canyon-dominated continental slope (van Haren et al., 2002). Like in the Bay of Biscay observations, the internal wave slope is not tight, and several small-range slopes are observed, e.g., near f and near N, that slope like −1 (Fig. 7). A −1-slope describes intermittency, pink noise (Schuster, 1984), and such a slope has been observed in open-ocean temperature spectra where turbulence levels are low and possibly representing a non-saturated internal wave field (van Haren and Gostiaux, 2009). Such a slope change may be attributed to varying N(x,y,z,t), which is more homogeneous and less affected by internal wave straining near the upper T-sensors compared with the lower T-sensors. The buoyancy frequency range is indicated by the horizontal bar in Fig. 7, but it is noted that it is less wide for the upper T-sensors and the distribution of its values, although non-Gaussian, peaks at N.

The buoyancy frequency range expanded around mean N not only includes propagating internal waves, but partially also turbulent overturns. After all, turbulent overturns may develop down to the largest possible local buoyancy scale (lowest buoyancy frequency N_{min} in near-homogeneous layers that need to last sufficiently long for the slowest overturn to develop) and internal waves up to the smallest possible buoyancy scale (largest buoyancy frequency $N_{s,max}$ in thin strongly stratified layers). While it is clear that for ($f \leq$) $\omega < N_{min}$ internal waves dominate as turbulence cannot exist, and that for $\omega > N_{s,max}$ turbulent motions dominate (provided the relevant overturning Ozmidov-scales L_O are resolved by the instrumented line), it is unclear what signals dominate in the range between. Such signals will contain a transition from internal waves to stratified anisotropic turbulence to isotropic turbulence. In Fig. 8 we investigate this transition for the two examples of data presented in Figs. 5, 6.

The temperature variance spectra in Fig. 8a,c are scaled with the turbulence inertial subrange that slopes with frequency as $\omega^{-5/3}$ (Tennekes and Lumley, 1972). For upper layer T-sensors and $\omega >$ ($\omega_O \geq$) $N_{s,max}$, the scaled spectra are observed to slope like −1/3 in the log–log plot, which is a slope of −2 in unscaled plotting. Here, $\omega_O = U/L_O$ denotes the Ozmidov frequency that separates the buoyancy range of stratified anisotropic quasi-2D turbulence at $\omega < \omega_O$, and the inertial subrange of isotropic 3D turbulence at $\omega > \omega_O$. These spectra thus do not reach the flat level (slope 0) of inertial subrange of isotropic turbulence for a passive scalar (Warhaft, 2000). In the present data, ω_O is not well computed using the observed mean current flow speed, because the

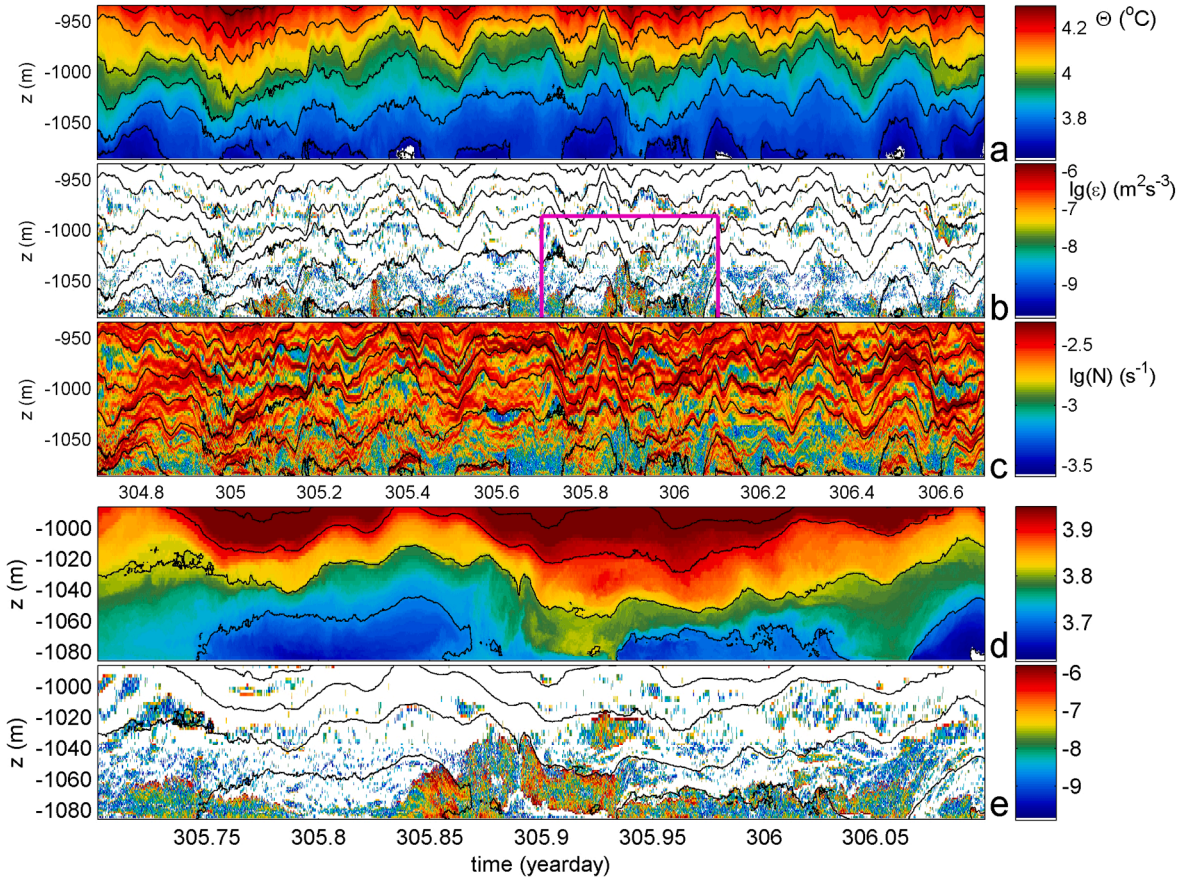

Fig. 6. As Fig. 5, but for a period with higher frequency internal wave dominance, one month later.

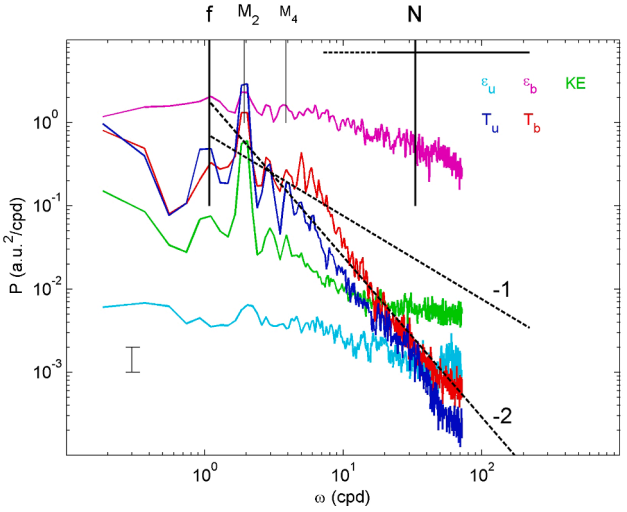

Fig. 7. Variance spectra from 10 min sub-sampled time series of upper (blue) and lower (red) T-sensors, 30 sensor-averaged turbulence dissipation rate for upper (light-blue) and lower (purple) ranges, and kinetic energy for 10 min sampled ADCP-data from z = −960 m (green). The spectra are arbitrarily shifted vertically because of the different units of the variables. Vertical black lines indicate inertial f, semidiurnal lunar tidal M_2, quarter-diurnal lunar M_4 and mean large-scale buoyancy N frequencies. The horizontal black line indicates the buoyancy frequency extent from minimum, in weakly stratified layers (the dashed portion has insufficient long duration for complete turbulent overturning), to maximum values, in small-scale strongly stratified layers. The dashed sloping lines indicate frequency (ω) scaling laws ω^{-1} and ω^{-2} (see text). (For interpretation of the references to colour in this figure legend, the reader is referred to the web version of this article.)

ADCP was not on the same mooring line as the T-sensors and, more importantly, the 300 kHz instrument did not reach deep enough in the water column. Also, mean $L_O = 1$ m for the upper layer and thus not well-resolved using the vertical separation between sensors.

For the lower layer, mean $L_O = 5$ m and well resolved by the sensors. The inertial subrange is found with slope 0 in both scaled log–log plots of Fig. 8a,c for $\omega > N_{s,max}$. At $N < \omega < N_{s,max}$, there is some tendency for different slopes between −1 (or + 2/3 in Fig. 8a,c) and −7/5 (+4/15 in Fig. 8a,c). The latter slope indicates convective turbulent overturning of an active scalar (Pawar and Arakeri, 2016), but it is not very clear in the present data. Evidently, there is a large difference in spectral slope between upper and lower layers, demonstrating more shear-induced turbulence that governs an inertial subrange in the lower layer (Warhaft, 2000).

At the maximum small-scale buoyancy frequency, which coincides with the lower layer ω_O, the mean coherence 'coh' between all possible pairs of independent T-sensors of the cross-correlation $[T(z)T(z + \Delta z)]/[T^2]$ at $\Delta z = 2$ m intervals is approximately coh = 0.5 ± 0.1, with larger values for the lower layer for which coherence does not drop off steeply at $\omega > N$ compared with the upper layer. The 95% significance level is at coh = 0.2 At N, coherence values are > 0.9. This may be interpreted as coherent structures shrinking to smaller than 2-m in the vertical for frequencies higher than $N_{s,max}$.

3.5. Vertical turbulence profiles

The spectral information of more prominent temperature variance at super-buoyancy frequencies that are associated with shear-induced turbulence observed near the seafloor is reflected in the two-day mean vertical turbulence dissipation rate profiles (Fig. 9a). Although some variation is observed between the two profiles, with slightly larger

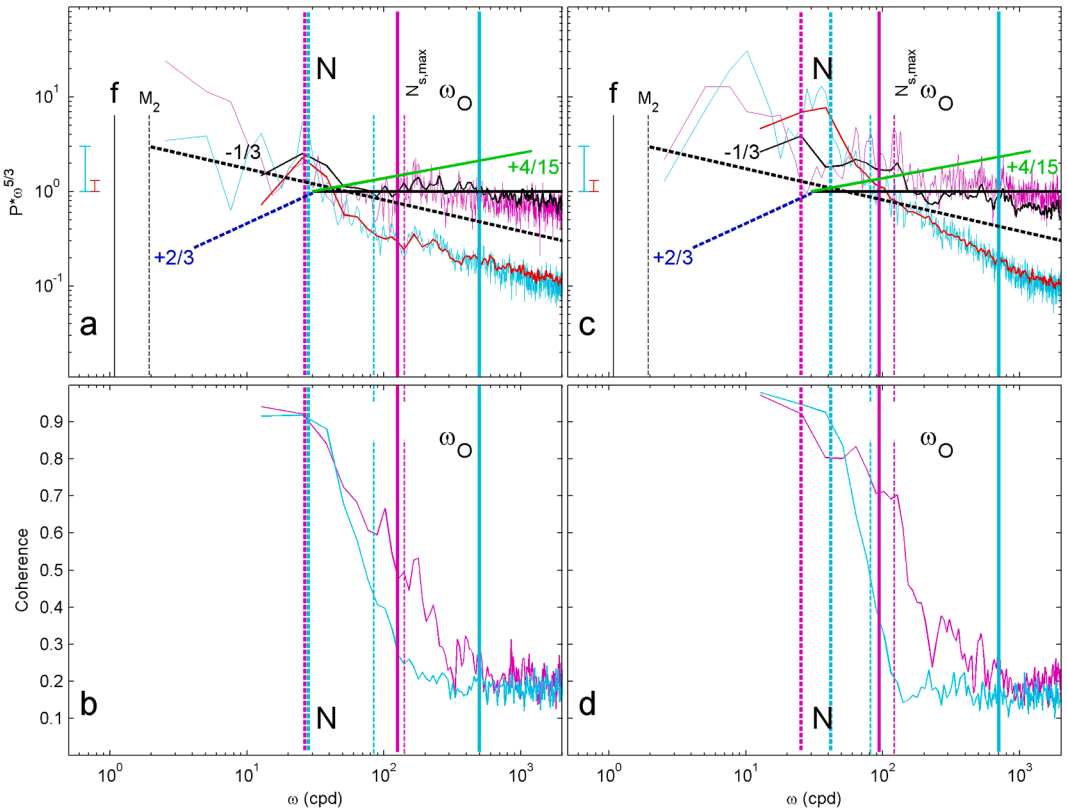

Fig. 8. Temperature spectra for 10-h data from lower and upper 30 T-sensor data groups (purple/black and light-blue/red, respectively). (a) Log-log plot of mean temperature variance for data from Fig. 5c scaled with the inertial subrange slope −5/3 (horizontal black line) for nearly raw (10 degrees of freedom 'dof'; thin lines) and moderately smoothed (50 dof; thick lines). Vertical color lines indicate the associated N (thick-dashed) and $N_{s,max}$ (thin-dashed) as well as the Ozmidov frequencies ω_O (thick-solid) for both data sets. The sloping lines show several deviations from the inertial subrange (see text). Spectral roll-off due to data-spikes starts at about 1000 cpd > ω_O. (b) Mean coherence between all possible pairs of 2-m separated T-sensors for the same upper and lower data groups as in a. The 95% significance level is at coh = 0.2. (c) As a., but for data of Fig. 6c. All slopes are identical as in a., for reference, but vertical lines show locally calculated values. (d) As b., but for data-groups of c.

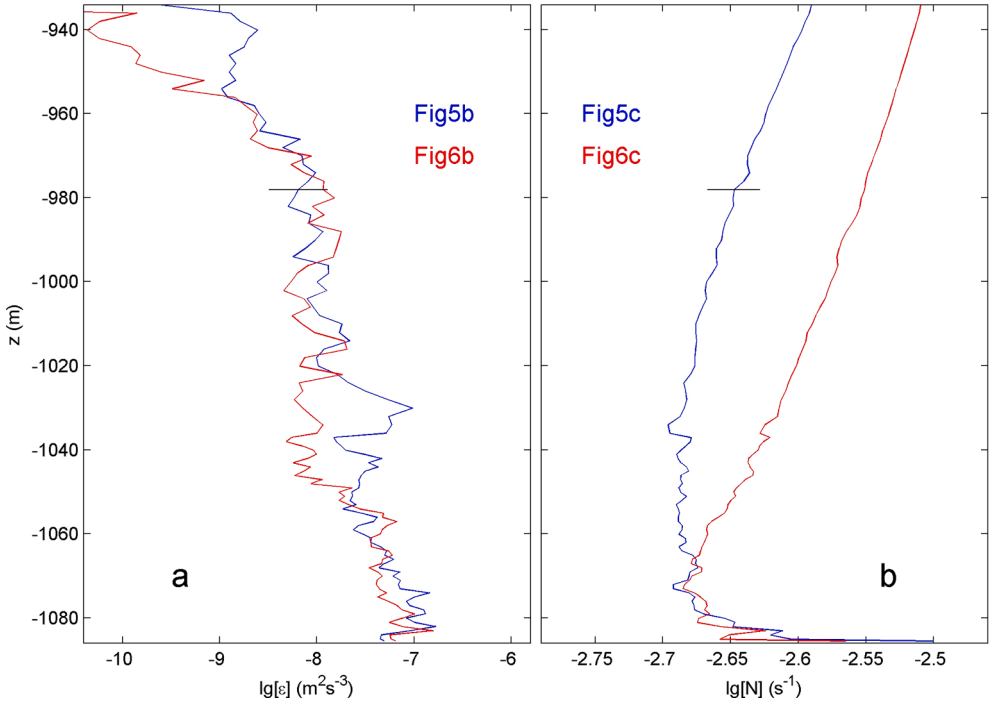

Fig. 9. Two-day mean vertical profiles for moored T-sensor data in Figs. 5, 6. (a) Logarithm of dissipation rate. (b) Logarithm of buoyancy frequency from reordered profiles.

values for the Fig. 5b-profile, the two are generally not significantly different. However, their vertical structure, with a two-orders of magnitude almost monotonic increase with depth, is significant. Largest dissipation is thus found near the seafloor, with no indication of a significant decrease to low values towards the seafloor. The turbulence works against vertically almost constant mean stratification (Fig. 9b; the x-axis range is only half an order of magnitude wide), despite the considerable temporal variability in Figs. 5c, 6c, with minimum mean values about 10–15 m above the seafloor and relatively strong increase in values towards the seafloor. As a result, the observed turbulence is not related to bottom-frictional flow, which tends to zero-turbulence at the boundary, and the turbulent mixing is expected to be efficient because a well-mixed near-homogeneous 'bottom-boundary layer' with $N < f$ is not observed.

4. Discussion and conclusions

Modelling efforts have demonstrated the capability of strong and effective turbulent mixing above sloping topography due to the breaking of internal waves. Gemmrich and Klymak (2015) used a numerical model on internal wave motions over sloping topography without bottom friction to demonstrate that turbulence was largest at the seafloor (of a critical slope). Winters (2015) let internal (tidal) waves slosh against a super-critical slope to demonstrate the continuous restratification and thus effective mixing occurring every wave period, also very close to the seafloor. Results from these 2D-models include mean turbulence dissipation rates that are largest near the seafloor, as observed in our data with largest mean turbulence dissipation rate around the lowest instrument, at 0.5 m from the seafloor. This also implies that turbulent (heat) fluxes are largest near the seafloor.

The observed lack of mean near-zero-N above the sloping seafloor confirms the continuous restratification and is associated with efficient mixing. Although the precise processes governing such maximum ε near the seafloor are unknown, the dominance of internal wave breaking may direct to 3D-processes, both above a smooth 2D-slope like in the present observations as above a 3D-slope like a canyon-incised continental slope.

The present estimated turbulence dissipation rates are about half an order of magnitude smaller than other estimates of breaking internal waves above various deep-sea sloping topography where freely propagating semidiurnal internal tides dominate and break at super-critical slopes (e.g., van Haren and Gostiaux, 2012). This may be attributable to an observed lack of upslope propagating bores, which are commonly observed above large just supercritical slopes, and/or hydraulic jumps, which mainly occur near crests of seamounts. Why these processes are not developing in the present two-month record is unknown. Possibly, the nearness of the sub-critical slope, less than one internal tidal wavelength from the mooring site, may cause the lack of development of such strong nonlinear motions. However, at the 2500 m deep foot of Rockall Bank in the East-Atlantic acoustic and current bursts have been observed that suggest bores to occur (Bonnin et al., 2006).

For future use we recommend to use lower frequency ADCP's in deep-sea waters and to have ADCP's in each mooring line including that with T-sensors. This enables to compute gradient Richardson and Froude numbers and to more precisely establish the mean Ozmidov length-scales across most of the range of the T-sensors, except close to the seafloor due to side-lobe reflection. Technically, the release-frame worked very well and confirms that a free-falling mooring line, descending at a speed of 1 to 1.5 m s^{-1}, slacks only a few centimeters before straining its mooring cable upon landing. As a result, when the seafloor texture is known to be smooth, a short anchor-release chain may be used.

Declaration of Competing Interest

The authors declare that they have no known competing financial interests or personal relationships that could have appeared to influence the work reported in this paper.

Acknowledgments

We thank captain and crew of the R/V Sproul and Scripps IO and WHOI technicians for their assistance in deploying and recovering the moorings. NIOZ-NMF technicians helped preparing the T-sensor mooring and manufactured the release-frame. M. Stastna (Univ. Waterloo, Canada) provided the darkjet colourmap suited for our data. This work has been partially funded from NSF-grant OCE-1756264.

References

Armi, L., 1978. Some evidence for boundary mixing in the deep ocean. J. Geophys. Res. 83 (C4), 1971. https://doi.org/10.1029/JC083iC04p01971.
D'Asaro, E.A., Lien, R.-C., 2000. The wave-turbulence transition for stratified flows. J. Phys. Oceanogr. 30 (7), 1669–1678.
Bonnin, J., Van Haren, H., Hosegood, P., Brummer, G.-J., 2006. Burst resuspension of seabed material at the foot of the continental slope in the Rockall Channel. Mar. Geol. 226 (3-4), 167–184.
Chalamalla, V.K., Sarkar, S., 2015. Mixing, dissipation rate, and their overturn-based estimates in a near-bottom turbulent flow driven by internal tides. J. Phys. Oceanogr. 45, 1969–1983.
Dewey, R.K., Crawford, W.R., Gargett, A.E., Oakey, N.S., 1987. A microstructure instrument for profiling oceanic turbulence in coastal bottom boundary layers. J. Atmos. Ocean. Technol. 4 (2), 288–297.
Dillon, T.M., 1982. Vertical overturns: a comparison of Thorpe and Ozmidov length scales. J. Geophys. Res. 87 (C12), 9601. https://doi.org/10.1029/JC087iC12p09601.
Ekman, V.W., 1905. On the influence of the Earth's rotation on ocean-currents. Ark. Math. Astron. Fys. 2 (11), 1–51.
Ferrari, R., Mashayek, A., McDougall, T.J., Nikurashin, M., Campin, J.-M., 2016. Turning ocean mixing upside down. J. Phys. Oceanogr. 46, 2239–2261.
Galbraith, P.S., Kelley, D.E., 1996. Identifying overturns in CTD profiles. J. Atmos. Ocean. Tech. 13 (3), 688–702.
Garrett, C., 1990. The role of secondary circulation in boundary mixing. J. Geophys. Res. 95 (C3), 3181. https://doi.org/10.1029/JC095iC03p03181.
Garrett, C., Munk, W., 1972. Space-time scales of internal waves. Geophys. Fluid Dyn. 3 (3), 225–264.
Gemmrich, J., Klymak, J.M., 2015. Dissipation of internal wave energy generated on a critical slope. J. Phys. Oceanogr. 45, 2221–2238.
Gregg, M.C., 1987. Diapycnal mixing in the thermocline. J. Geophys. Res. 92, 5249–5286.
Gregg, M.C., D'Asaro, E.A., Riley, J.J., Kunze, E., 2018. Mixing efficiency in the ocean. Ann. Rev. Mar. Sci. 10 (1), 443–473.
Hosegood, P., Bonnin, J., van Haren, H., 2004. Solibore-induced sediment resuspension in the Faeroe-Shetland Channel. Geophys. Res. Lett. 31 (9), L09301. https://doi.org/10.1029/2004GL019544.
IOC, SCOR, IAPSO, 2010. The international thermodynamic equation of seawater – 2010: Calculation and use of thermodynamic properties. Intergovernmental Oceanographic Commission, Manuals and Guides No. 56, UNESCO, Paris, France, 131 pp.
Lerczak, J.A., Winant, C.D., Hendershott, M.C., 2003. Observations of the semidiurnal internal tide on the southern California slope and shelf. J. Geophys. Res. 108, 3068.
Kim, S.Y., 2010. Observations of submesoscale eddies using high-frequency radar-derived kinematic and dynamic quantities. Cont. Shelf Res. 30 (15), 1639–1655.
Klymak, J.M., Pinkel, R., Rainville, L., 2008. Direct breaking of the internal tide near topography: Kaena Ridge, Hawaii. J. Phys. Oceanogr. 38, 380–399.
LeBlond, P.H., Mysak, L.A., 1978. Waves in the Ocean. Elsevier, New York, NY, USA, p. 602.
Li, S., Li, H., 2006. Parallel AMR code for compressible MHD and HD equations. T-7, MS B284, Theoretical division, Los Alamos National Laboratory, http://citeseerx.ist.psu.edu/viewdoc/summary;jsessionid=6E3D6C8D28DD3CAE8E5CBC825EB6385C?doi=10.1.1.694.3243 (last accessed: 14 November 2021).
Mater, B.D., Venayagamoorthy, S.K., St. Laurent, L., Moum, J.N., 2015. Biases in Thorpe scale estimation of turbulence dissipation. Part I: Assessments from large-scale overturns in oceanographic data. J. Phys. Oceanogr. 45, 2497–2521.
Mashayek, A., Caulfield, C.P., Alford, M.H., 2022. Goldilocks mixing in oceanic shear-induced turbulent overturns. J. Fluid Mech. 928, 1–32.
Matsumoto, Y., Hoshino, M., 2004. Onset of turbulence by a Kelvin-Helmholtz vortex. Geophys. Res. Lett. 31, L02807. https://doi.org/10.1029/2003GL018195.
Mazloff, M.R., Cornuelle, B., Gille, S.T., Wang, J., 2020. The importance of remote forcing for regional modeling of internal waves. J. Geophys. Res. 125, e2019JC015623.
Munk, W.H., 1966. Abyssal recipes. Deep-Sea Res. 13 (4), 707–730.
Munk, W., 1981. Internal waves and small-scale processes. In: Warren, B.A., Wunsch, C. (Eds.), Evolution of Physical Oceanography. MIT Press, Cambridge, MA, USA, pp. 264–291.
Nash, J.D., Alford, M.H., Kunze, E., Martini, K., Kelly, S., 2007. Hotspots of deep ocean mixing on the Oregon continental slope. Geophys. Res. Lett. 34, L01605. https://doi.org/10.1029/2006GL028170.

Oakey, N.S., 1982. Determination of the rate of dissipation of turbulent energy from simultaneous temperature and velocity shear microstructure measurements. J. Phys. Oceanogr. 12 (3), 256–271.
Pawar, S.S., Arakeri, J.H., 2016. Kinetic energy and scalar spectra in high Rayleigh number axially homogeneous buoyancy driven turbulence. Phys. Fluids 28 (6), 065103. https://doi.org/10.1063/1.4953858.
Pinkel, R., Alford M.H., 1999. Internal wave energetics at a seamount on the California Continental Borderland. In: Müller, P., Henderson, D. (Eds.), Dynamics of Oceanic Internal Gravity Waves, II, Proceedings, 'Aha Huliko'a Hawaiian Winter Workshop University of Hawaii at Manoa, January 18-22 1999, 21-28.
Ponte, A.L., Cornuelle, B.D., 2013. Coastal numerical modelling of tides: Sensitivity to domain size and remotely generated internal tide. Ocean Mod. 62, 17–26.
Prandtl, L., 1905. Über Flüssigkeitsbewegung bei sehr kleiner Reibung. Verhandl III, Intern. Math. Kongr. Heidelberg 1904, 484-491. Also in: Gesammelte Abhandlungen, 575-584.
Schuster, H.G., 1984. Deterministic Chaos, an Introduction. Physik-Verlag, Weinheim, Germany, p. 220.
Slinn, D.N., Riley, J.J., 1996. Turbulent mixing in the oceanic boundary layer caused by internal wave reflection from sloping terrain. Dyn. Atmos. Oceans 24 (1-4), 51–62.
Smyth, W.D., Moum, J.N., Caldwell, D.R., 2001. Efficiency of mixing in turbulent patches: Inferences from direct numerical simulations and microstructure observations. J. Phys. Oceanogr. 31, 1969–1992.
Tennekes, H., Lumley, J.L., 1972. A First Course in Turbulence. The MIT Press, Cambridge, MA, USA, p. 293.
Thorpe, S.A., 1977. Turbulence and mixing in a Scottish loch. Phil. Trans. Roy. Soc. Lond. A 286, 125–181.
Thorpe, S.A., 1987. Current and temperature variability on the continental slope. Phil. Trans. Roy. Soc. Lond. A 323, 471–517.
van Haren, H., 2006. Nonlinear motions at the internal tide source. Geophys. Res. Lett. 33, L11605. https://doi.org/10.1029/2006GL025851.
van Haren, H., 2018. Philosophy and application of high-resolution temperature sensors for stratified waters. Sensors 18, 3184. https://doi.org/10.3390/s18103184.
van Haren, H., Gostiaux, L., 2009. High-resolution open-ocean temperature spectra. J. Geophys. Res. 114, C05005. https://doi.org/10.1029/2008JC004967.
van Haren, H., Gostiaux, L., 2012. Detailed internal wave mixing above a deep-ocean slope. J. Mar. Res. 70 (1), 173–197.
van Haren, H., Oakey, N., Garrett, C., 1994. Measurements of internal wave band eddy fluxes above a sloping bottom. J. Mar. Res. 52 (5), 909–946.
van Haren, H., Maas, L., van Aken, H., 2002. On the nature of internal wave spectra near a continental slope. Geophys. Res. Lett. 29 (12), 1615. https://doi.org/10.1029/2001GL014341.
Warhaft, Z., 2000. Passive scalars in turbulent flows. Ann. Rev. Fluid Mech. 32 (1), 203–240.
Winters, K.B., 2015. Tidally driven mixing and dissipation in the boundary layer above steep submarine topography. Geophys. Res. Lett. 42, 7123–7130. https://doi.org/10.1002/2015GL064676.